Mechanical properties of cellular ceramics obtained by gel casting: Characterization and modeling

C. Bartuli [a,*], E. Bemporad [b], J.M. Tulliani [c], J. Tirillò [a], G. Pulci [a], M. Sebastiani [b]

[a] *Dept. of Chemical Engineering Materials Environment, Sapienza University of Rome, via Eudossiana 18, 00184 Rome, Italy*
[b] *Dept. of Mechanical and Industrial Engineering, University of Roma 3, Via della Vasca Navale 79, 00146 Rome, Italy*
[c] *Dept. of Materials Science and Chemical Engineering, Politecnico di Torino, Corso Duca degli Abruzzi 24, 10129 Torino, Italy*

Abstract

Dense and cellular ceramics were produced from yttria partially stabilized zirconia powders by gel-casting, using agar as a gelling agent and polyethylene spheres (125–300 μm diameter) as volatile pore forming agent to create 50–65 vol.% spherical macropores, uniformly distributed in a microporous matrix.

The mechanical properties of both dense and porous samples were investigated at the microscale by nanoindentation testing. The influence of micro-porosity on the mechanical properties of samples was evaluated by the analysis of hardness and modulus depth profiles, coupled with FIB-SEM section observations of selected indentation marks. The intrinsic elastic modulus of the zirconia phase resulted to be of the order of 220 GPa. Mechanical characterization at the macroscale consisted of uniaxial compression tests and four point bending tests. Elastic moduli of about 170 GPa were measured for about 93% dense ceramics, lowering down to 44 and 13 GPa with the addition 50 and 65 vol.% macropores, respectively. Digital image based finite element analysis (DIB-FEA) procedures were implemented in order to verify their applicability for the prediction of mechanical behavior of this type of cellular materials: results confirmed that a very good match between measured and calculated values of elastic modulus can be achieved, provided that the effects of micro-porosity are considered by the proper choice of the elastic properties to be assigned to each individual phase identified by Image Analysis.
© 2009 Elsevier Ltd. All rights reserved.

Keywords: Gel casting; Cellular ceramics; DIB-FEA; Partially stabilized zirconia; Nanoindentation

1. Introduction

Porous and cellular ceramic materials are the object of considerable interest since specific competitive functionalities (such as increased surface area, permeability, heat transfer capacity, or maximized strength/density ratio) can be provided to the correspondent solid materials by the presence of a controlled amount and distribution of "voids".[1] These properties are responsible for increasingly wide application of these materials for a variety of chemical, industrial or biological processes, such as molten metals filtration, high-temperature thermal insulation, support for catalytic reactions, filtration of particulates from diesel engine exhaust gases and of hot corrosive gases, and bio-compatible scaffolds for bone substitution.[2,3]

All mentioned properties, with particular reference to mechanical behavior and thermal properties of the porous bodies, are strongly affected by their specific microstructural features, the latter being determined by manufacturing processes[4,5]: shape, dimension and distribution of cavities and pores, together with their interconnection and orientation, play for example a decisive role in determining strength, creep and thermal fatigue resistance, thermal conductivity and expansion coefficient and permeability of cellular or porous ceramic bodies. It is therefore extremely important to identify consistent predictive models that can reliably assess the consequences of microstructural variations induced by modifications of the fabrication process on the mechanical behavior of real components.

Mechanical behavior of cellular solids has been extensively studied and a variety of models have been proposed in order to describe it. Gibson and Ashby,[6] in particular, have given the most important contribution to the construction of the theoretical basis for calculating the stress and strain fields inside cellular solids.

* Corresponding author. Tel.: +39 06 6892568; fax: +39 06 6876343.
E-mail address: bartuli@uniroma1.it (C. Bartuli).

The importance of all microstructural details including, not only the total amount of pores but also the shape of the cells, the cell window opening, the number, shape and size of interconnections between pores, the degree of anisotropy and the surface/volume ratio, have been widely recognized. However, the most commonly accepted approaches to the finite element modeling of porous materials are based on the adoption of numerous simplifying hypotheses. A comprehensive review of different methodologies to the mechanical modeling of cellular solids is reported in Ref. [7]. The main general assumption is that of a uniform spatial distribution of cavities and pores: the real material is modeled as a repetitive spatial structure of elementary cells (minimum volume), whose walls are commonly modeled as beams or struts.[8] That strategy, however, can only be applied when the shape and distribution of cavities is regular all over the total volume, but this hypothesis is not often verified, so that the results obtained can provide only averaged values for the parameters of interest.

A different approach, aimed to design a model able to reply as accurately as possible the microstructure of porous materials, is based on digital image based finite element modeling (DIB-FEA).[9–11] The general idea is that of building up a finite element model that includes all the relevant microstructural features starting directly from real micrographs of its cross-sections, and carrying out structural and functional analyses on the designed model. Specific softwares have already been designed that can follow such methodology: one in particular, OOF (object oriented finite element analysis)[12,13] has been developed by NIST and has been used proficiently for predicting the mechanical and thermal properties of a large range of materials[14,15]: the software is made freely available, along with the source code, for scientific purposes.[16]

The possibility of taking into account the actual morphology of the microstructural features for a reliable finite element simulation is of particular interest in the cases where the response of the investigated system is strongly dependent upon geometrical parameters, so that consistent process parameters → actual shape → macroscopic properties correlations can be developed. It is evident that the study of the mechanical response of ceramic porous or cellular materials represents one of these cases, and that these materials can be assimilated to biphasic structures where one of the phases, present in amounts of the same magnitude of the second phase, is represented by voids.

Even though DIB-FEA techniques are at present widely adopted for the mechanical modeling of multiphase materials, several problems related to the assessment of reliability, robustness and statistical validity of obtained results still remain unsolved: in particular, the most critical point seems to be the proper selection of the relevant microstructural features (i.e. of the characteristic scale) to be considered in the finite element model, in the optics of the optimization of computing resources. Further work is still necessary in the definition of the most appropriate procedure for the correct microstructural modeling of inhomogeneous brittle materials and structures. The present paper proposes a multiscale integrated approach for the mechanical characterization of dense and porous ceramic bodies produced by gel casting, based on macro- and micro-mechanical testing and high resolution microstructural characterization, coupled with OOF modeling of the produced structures.

Gel casting is a wet forming method based on the combination of ceramic processing and polymer chemistry. This process involves the dispersion of a ceramic powder into a monomer solution and the casting of this suspension into a non-porous mould. Polymerization is then promoted and consequently ceramic particles are entrapped into the rigid and homogenous polymeric network.[17] After gel formation, gel-cast green materials can be easily demolded and are then dried in controlled conditions. Gel-casting process can be modified to fabricate porous ceramics by combining it with foaming techniques, or replica methods, or even with the addition of a sacrificial phase.[2,18]

In this paper, a fugitive phase, made of commercial polyethylene spheres in a size range selected by sieving, was added to the ceramic suspension in agar before gelling and sintering. The shape, size and size distribution of these spheres as well as their volume fraction with respect to the ceramic content into the slurry can allow a strict control of many porosity features of the final components.

Dense and porous (about 50–60% of theoretical density) yttria partially stabilized zirconia samples were produced in the shape of cylinders and prismatic bars.

Samples were characterized for microstructure and resistance to compression and bending, evaluating both elastic modulus and modulus of rupture. Hardness and elastic modulus measurements were also performed on both dense and porous specimens by nanoindentation.

Results of mechanical and microstructural characterization were used to integrate and validate the DIB-FEA model, assessing the influence of the level of detail adopted for the simulation of the microstructure on the accuracy of the calculation, and assisting the final decisions about the degree of refinement of the geometrical mesh.

2. Materials and experimental methods

2.1. Gel casting technique

Commercial stabilized zirconia with 3 mol% yttria (yttria tetragonal zirconia polycrystal, Y-TZP, grade TZ-3YS supplied by Tosoh Co., Japan) was used for preparation of ceramic suspensions. Particle size distribution was determined by means of a laser granulometer (Fristch Analysette 22) in ethanol after 10 min of ultrasonication: the mean diameter of the zirconia powder was about 0.6 μm, while the diameters corresponding to 10% and 90% of the particle size distributions were respectively 0.33 and 1 μm.

Two different kinds of agar were chosen as gelling agents: gum agar Fluka 05040 and Sigma–Aldrich 07049; they were dissolved in hot water at about 90 °C and gelled on cooling.[19] After calcination, the declared residual ash fraction were ≤6% and 2%, respectively for Fluka and Sigma–Aldrich products.

A polyethylene (PE) powder (Clariant Italia SpA) having a density at 23 °C of about 0.92–0.94 g/cm³ was used as fugitive phase. Its thermal decomposition is almost completed

after calcination at 550 °C.[20] PE powder was made of almost spherical particles, but irregular structures were also present.[21] Polyethylene spheres were sieved in the range 125–300 μm before dispersion into ceramic suspensions.

To set-up the gelling/sintering procedure dense components were produced. With the Fluka agar, suspensions having a powder content of 55.35 wt.% were prepared in deionized water containing Dolapix PC 33 (Zschimmer & Schwarz, 1.22 wt.% respect to zirconia powder) as a dispersant; with the Sigma–Aldrich agar, suspensions having a higher solid content of 58.82 wt% could be prepared in deionized water with the same dispersant content. Part of the water was used to disperse the zirconia powder with Dolapix (45 min magnetic stirring, 15 min ultrasonication). The agar was dissolved into the remaining part of the deionized water at 90 °C for 1 h (2.38 wt.% of agar in this suspension) and this solution was then cooled down to 60 °C and added to the ceramic suspension warmed at the same temperature under magnetic stirring.

Agar favors foam formation during preparation,[22] therefore a de-airing step was required to remove air bubbles entrapped into the ceramic suspensions. Casting of the suspensions made with the Fluka agar was carried out under vacuum (about 10^{-2} Pa). Slurries were poured into non-porous Plexiglas moulds at 60 °C. Cylindrical moulds having different dimensions (internal diameter from 12 up to 18 mm and height in the range 30–55 mm) as well as 10 mm × 10 mm × 90 mm bars were used. Cooling down to room temperature promoted gelification.

To fabricate porous ceramics, PE spheres were added to the powder suspensions after preliminary dispersion in water, in suitable amounts to obtain zirconia bodies having about 40 and 50 vol.% porosity. The ceramic content of the slurries was the same adopted for the dense materials.

All cast samples were initially slowly dried at room temperature under a controlled humid atmosphere; after demolding drying was completed in static air. Final sintering at 1550 °C was carried out for one hour (Fluka agar) or 2 h (Sigma–Aldrich agar).

2.2. Characterization procedures

2.2.1. Morphological and microstructural characterization

Digital optical microscopy (DOM) was adopted for the morphological characterization of porous bodies, using a purposely developed procedure. Images acquired by Optical Microscopy (2560 × 1920 pixel resolution) were processed using a cascade of filters according the following procedure: contrast equalization, threshold, binarization, mean, ranking, morphological closing. Detected voids were classified on the basis of their area and other geometrical parameters (mean porosity, porosity distribution, circularity, mean shape factor, average chord, maximum Feret's diameter) are then calculated. This procedure was repeated on 5 different micrographs for an overall investigated area of 7 mm².

Microstructural analysis and sub-surface micro-porosity evaluation were performed by focused ion beam (FIB) technique, coupled with FEG-SEM observations (FEI Helios NanoLab 600 Dual Beam). Cross-sections were obtained by FIB milling after a preliminary *in situ* platinum deposition to protect surface layers during ion milling; the sectioning process consisted of a preliminary high ion current milling (9 nA) followed by a cleaning step of the section (0.9 nA) until the desired section was obtained.

Microstructural observation was performed both using the ion probe (maximum microstructural contrast) and the electron probe (maximum morphological contrast), secondary electrons in both cases.

2.2.2. Mechanical characterization

Dense and porous specimens were characterized at the macroscale by monotonic uniaxial compressive tests (elastic modulus and compressive strength) and four point bending tests (elastic modulus and flexural strength) at room temperature.

Uniaxial loading tests were carried out according to ASTM C1424-99 specification using an INSTRON 8033 servo-hydraulic testing machine on cylindrical specimens (aspect ratio, length/diameter = 1.7, to avoid buckling), precision-machined to obtain sufficiently planar and parallel faces.

Flexural strength and bending elastic modulus were evaluated by four point bending tests performed according to ASTM C1161-02c specification using Zwick-Roell Z010 (for dense specimens) and Z2.5 (for porous specimens) electromechanical testing machines (Zwick-Roell, Ulm, Germany). Specimens were machined starting from gel cast forms in the shape of 3 mm × 4 mm × 50 mm parallelepipeds, with 45° chamfered edges.

All specimens were instrumented for elastic modulus evaluation with resistance strain gauges (HBM LY41-3/120, HBM, Darmstadt, Germany), located in the centerline of the cylinder and thermally balanced by an identical strain gauge mounted on a sample made of the same material (half-bridge configuration). In order to avoid any influence of the adhesive on the final measurement, inductive displacement gauges were used to calculate the extrados sample deformation according to the elastic line equation. All tests were carried out in displacement control, with a crosspiece velocity of 0.5 mm/min, leading to the rupture in less than 1 min, as specified by the mentioned ASTM standard. Data relative to applied load and measured displacement, sampled at 10 Hz, were elaborated for the calculation of the maximum rupture load and of elastic modulus.

Nanoindentation testing[23] was performed by means of a Berkovich diamond indenter, using a Nano Indenter G200 (Agilent Technologies), in a continuous stiffness measurement mode (CSM) under a constant strain rate of $0.05\,s^{-1}$ and a maximum load of 650 mN, according to ISO 14577-1-2 standard. A Poisson's ratio of 0.3 was adopted for modulus calculations. The elastic contact stiffness S was dynamically measured during indentation and continuous hardness/depth and reduced modulus/depth curves were obtained by the use of the following equations[23]:

$$E_r = \frac{\sqrt{\pi}}{2} \cdot \frac{S}{\sqrt{A}} \tag{1}$$

Table 1
Sets of samples produced by gel casting: volume percent of pore forming agents, type of agar (F = Fluka, SA = Sigma–Aldrich), shape of the specimens and density (calculated as % of the theoretical).

Set	Number samples	Vol. % pore forming agent	Agar	Shape	Density (%)
Dense	3	0	SA	Cylindrical	96.0 ± 1.7
Dense	7	0	SA	Prismatic bars	93.4 ± 1.2
P50-1	5	50	F	Cylindrical	59.6 ± 1.2
P50-2	9	50	SA	Cylindrical	63.3 ± 1.5
P50	13	50	SA	Prismatic bars	61.6 ± 2.3
P65	6	65	SA	Cylindrical	49.2 ± 1.5
P65	6	65	SA	Prismatic bars	49.3 ± 0.8

$$H = \frac{P}{A} \tag{2}$$

where A is the projected contact area, calculated after indenter calibration on certified fused silica reference sample,[23] and P is the applied load measured during indentation.

The elastic modulus of the tested samples can be estimated from the measured reduced modulus by the following equation:

$$\frac{1}{E_r} = \frac{(1 - \upsilon)^2}{E} + \frac{(1 - \upsilon_i)^2}{E_i} \tag{3}$$

where E_i and υ_i are the elastic modulus and Poisson's ratio of the indenter.

In this way, reliable data can be obtained even for penetration depth of the order of 50 nm, and the influence of the sub-surface micro-porosity on the measured elastic modulus and hardness can be determined.

Samples were polished before indentation by the use of diamond lapping films, 15, 6, 3 and 1 μm grades, 1 min each.

In case of porous samples, indentations were performed on clean areas, not affect by surface macroporosity.

2.3. Digital image-based finite element analysis

The typical procedure for carrying out a digital image-based finite element analysis can be divided in the following steps:

1. choice of a representative cross-section;
2. discretization of the domain corresponding to the imported digital image;
3. identification of the different phases and assignment of material properties;
4. setting of boundary conditions and loads, followed by solution.

The final target is to predict with a sufficient level of accuracy and reliability the properties of the material starting from a digital image of its cross-section and the properties of the single components.

Fields were computed with linear shape functions (element edges with nodes only at the end points were used[24]). A reliable simulation of the behavior of a 3D microstructure by means of planar elements can only be assured for symmetrical structures. In the present case, all the characteristic elements of

the microstructure (sintering residual micro-pores, macropores from pore forming spheres) have central symmetry.

3. Results and discussion

3.1. Production of samples

Dense samples containing Fluka agar only reached a density of 87%. Due to the poor densification of these samples and to the difficult dispersion the PE spheres inside these slurries, only few porous pieces were produced using this gelling agent, and they were labeled as set 1. The samples obtained with the purer agar (Sigma–Aldrich) reached much higher average densities. Table 1 resumes the main fabrication details and characteristics of different sets of samples produced by gel casting. Density was calculated as % of the theoretical density of yttria stabilized zirconia (6.05 g/cm^3). A certain amount of residual micro-porosity (7% in average) is systematically observed for dense samples, likely due to incomplete de-airing and sintering processes, as described in the previous chapters.

3.2. Morphological and microstructural characterization

Digital images of representative cross-sections of macroporous samples from three different cellular specimens (from sets P50-1, P50-2 and P65) are shown in Fig. 1(a), (c), and (e). The corresponding binarized images are reported in Fig. 1 (b), (d), and (f).

Results of the statistical analysis of porosity, as calculated by digital image analysis, are reported in Table 2: observing the void volume fraction values for the three considered sets of porous samples, it is clear how the Image Analysis based density evaluation systematically under-estimates porosity in compari-

Table 2
Significant statistical parameters identifying microstructural features of representative samples from different sets (average of 5 images per sample): pores geometrical characteristics.

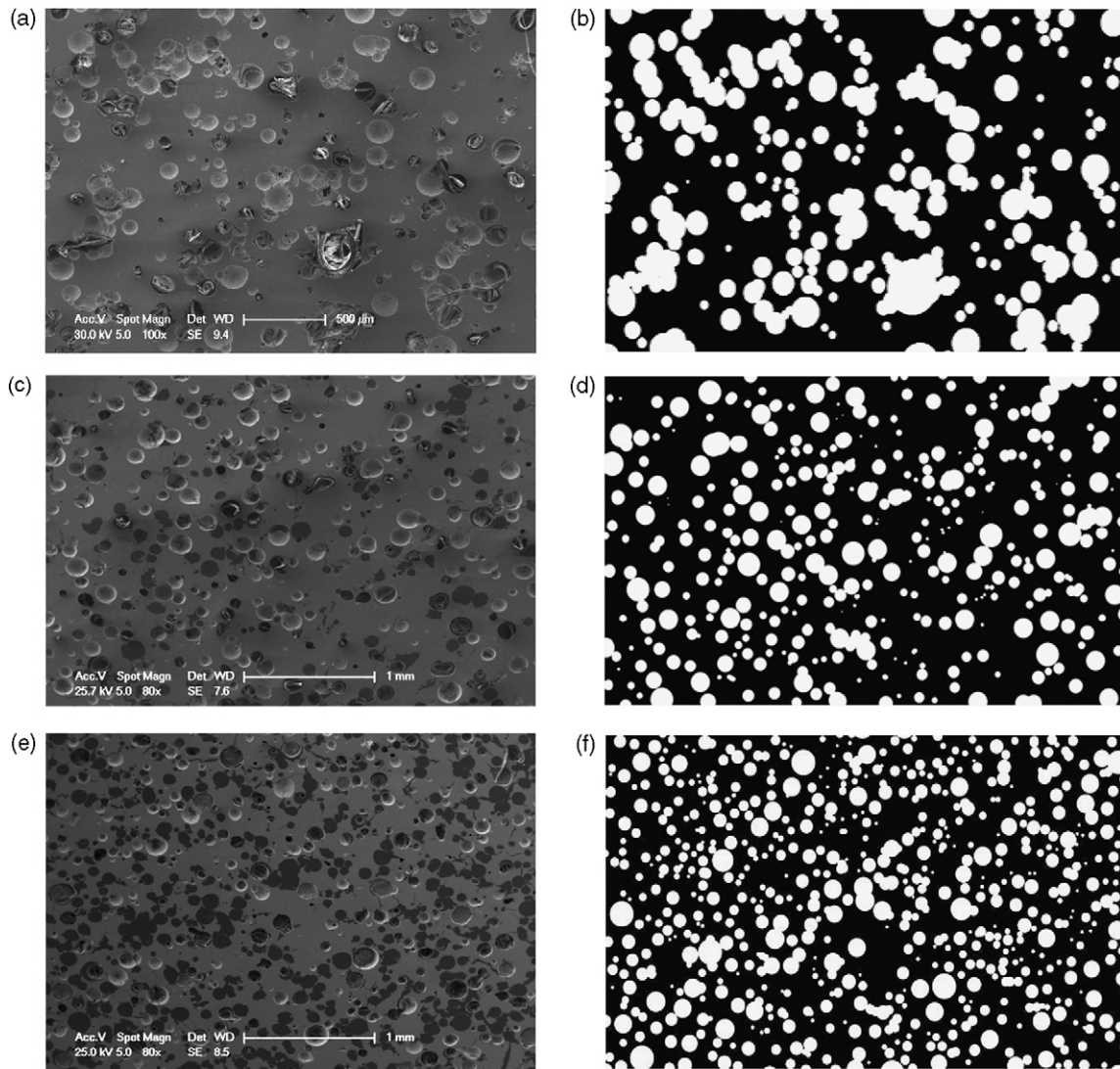| Parameters	P50 set 1	P50 set 2	P65
Volume fraction	0.35 ± 0.08	0.31 ± 0.09	0.42 ± 0.12
Average chord (μm)	71.6 ± 33.1	67.5 ± 26.1	55.0 ± 25.4
Circularity	0.8 ± 0.2	0.9 ± 0.13	0.9 ± 0.2
Feret maximum (μm)	135.2 ± 109.6	100.8 ± 51.9	87.8 ± 54.6
Shape factor	1.3 ± 0.5	1.2 ± 0.4	1.3 ± 0.5

Fig. 1. Representative cross-sections of three cellular specimens (from P50 set 1 (a); from P50 set 2 (c); from P65 (e); SEM micrographs) and corresponding binarized digital images (from P50 set 1 (b); from P50 set 2 (d); from P65 (f)).

son with results coming from the conventional weight/volume method. This experimental evidence confirms that the binarization process cannot take into account the presence of pores at microscale and nanoscale coming from the de-airing and sintering processes.

The spherical shape of the PE particle used as fugitive phase is maintained on sintering, and the average value of the macroporosity is very close to the initial volume percent of the pore generating agent. A strong tendency to sphere agglomeration was observed in case of sample set P50-1. Despite the high level of porosity resulting from a higher initial volume of pore forming spheres, samples from set P65 are characterized by optimal dispersion of the PE spheres.

Fig. 2(a)–(d) reports the FIB cross-sections microstructural analyses performed on both dense and porous samples. A common microstructure, consisting of fine hexagonal grains (200–500 nm), and a similar amount of micro-porosity were identified for both samples, confirming that porosity at the microscale is essentially due to the densification and sintering

processes, independently on the introduction of a pore forming agent. As a further evidence, Fig. 2(b) and (d) clearly show that the edges of the micro-pores are generated by the coalescence of adjacent grains. It is also significant that the actual shape of micro-pores is completely different from the spherical shape usually assumed for predicting failure and damage mechanisms of brittle materials.[25] The radius of curvature at the apex of the pores can be even lower than 20 nm: a significant local stress intensification factor with a direct influence on failure mechanisms and strength of both dense and porous bodies are therefore expected.

3.3. Mechanical characterization

Results of mechanical tests performed on dense, P50 (produced by adding 50 vol.% pore generating agent, set 1 and set 2) and P65 specimens (produced with 65 vol.% polyethylene spheres in the same conditions of P50 set 2) are resumed in Table 3 for both uniaxial compression and four point bending.
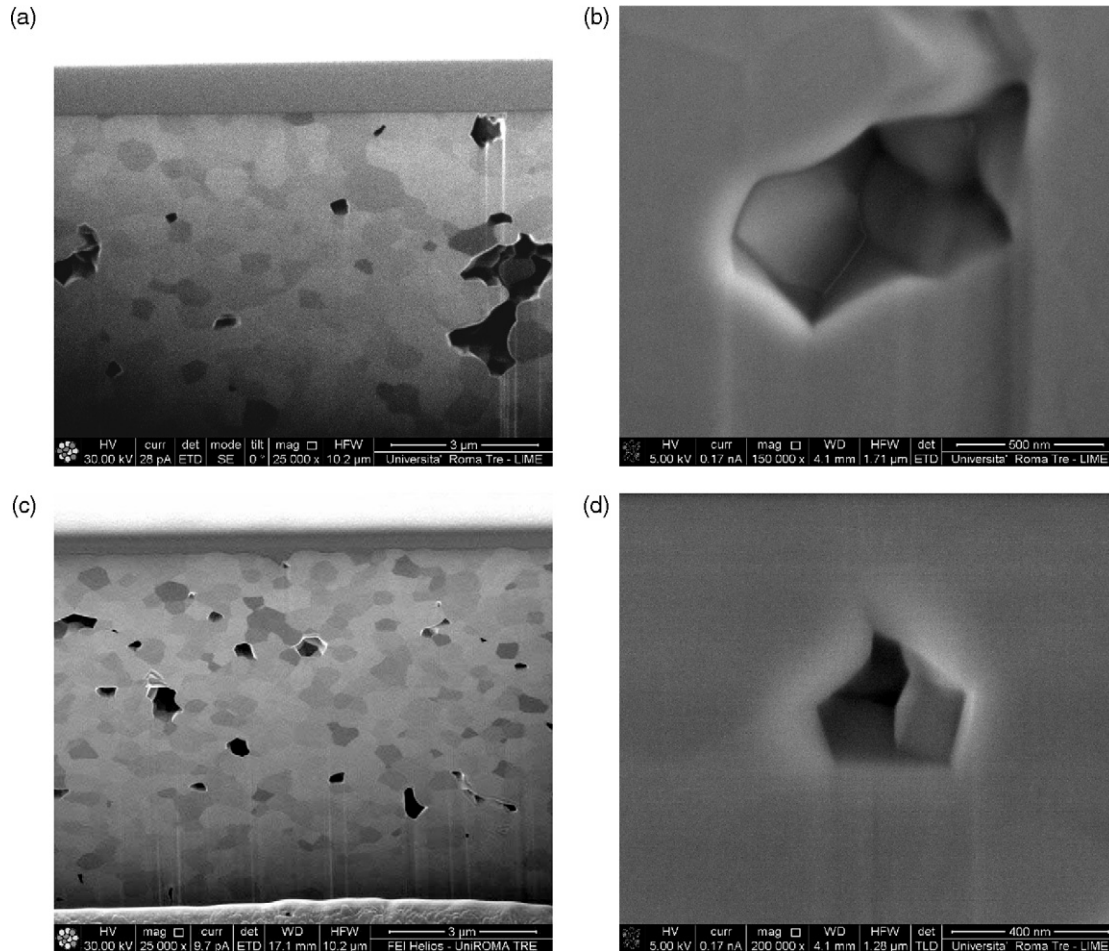
(a)

(b)

(c)

(d)

Fig. 2. SEM micrographs of FIB cross-sections of a dense sample (a, b) and a P50 porous sample (c, d), showing subsurface micro-porosity: (a, c) acquired using the ion probe and detecting emitted secondary electrons; (b, d) details acquired by the FEG-SEM column.

Compression tests performed on cylindrical dense samples could not lead to reliable results, since the measured values of the compression strength (an average of about 2 GPa) were too close to the maximum measurable strength of the employed machine. Moreover, a partial penetration of the samples inside the steel plates used for the loading was observed, so that the reliability of the modulus measurements could not be guaranteed.

Very similar compressive strengths (230 and 235 MPa) and a moduli (46 and 43 GPa) were measured for P50 specimens from set 1 and set 2. Compression elastic modulus falls down to 11 GPa when macro-porosity is increased to 65 vol.%.

During bending tests, dense material exhibited a perfectly elastic behavior, and brittle fraction was evidenced by the total absence of plastic deformation: the maximum measured strain was lower than 0.32%. An average value of 170 GPa was measured for the bending elastic modulus of dense specimens, with a limited standard deviation, confirming the homogeneity of dense samples. Average flexural strength is 413 MPa, with a larger standard deviation (110 MPa), as expected for brittle microporous materials obtained by sintering processes (presence of triple points).

For samples P50, fabricated in the same conditions of compression samples from set 2, the value of the elastic modulus

Table 3
Results of uniaxial compression and four point bending tests carried out on dense and porous samples: compressive strength, compression elastic modulus, flexural strength, bending elastic modulus (average ± standard deviation).

		Uniaxial compression		Four point bending	
		σ_{comp} (MPa)	E_{comp} (GPa)	σ_{flex} (MPa)	E_{bend} (GPa)
Dense		>2000[a]	–	413 ± 110	170 ± 6
P50	Set 1	230.2 ± 25.7	45.6 ± 5.8	33 ± 11	44 ± 9
	Set 2	235.5 ± 79.6	43.3 ± 15.4		
P65		38.3 ± 9.4	10.7 ± 3.5	12 ± 5	13 ± 8

[a] This value can only be considered as a rough estimation (see text).

Table 4
Results summary of nanoindentation tests: average ± standard deviation (Poisson's ratio = 0.3).

	Dense (density 96%)	Dense (density 93.5%)	P50 (density 62%)
Elastic modulus at penetration depth 100 nm [GPa]	219.00 ± 15.68	221.40 ± 30.62	238.10 ± 17.6
Elastic modulus at max penetration depth 1500 nm [GPa]	225.07 ± 6.35	177.28 ± 12.04	174.11 ± 6.6
Hardness at penetration depth 100 nm [GPa]	14.15 ± 1.66	14.6 ± 3.16	15.90 ± 1.4
Hardness at max penetration depth 1500 nm [GPa]	14.06 ± 0.77	12.82 ± 1.4	13.85 ± 0.53
Ratio between minimum and maximum measured hardness	0.994	0.878	0.871

was confirmed (44 GPa, about 26% of that of dense materials); the dispersion of experimental data was higher than that experienced by dense samples, due to the presence of a much higher number of possible crack origins. The load–deformation curves suggest a different mechanical behavior, deviating from linearity at higher loads and indicating the effect of collapse of the external walls of the macrocells.

For macroporous P65 samples the elastic modulus decreases down to 13 GPa (about 7% of the dense material), and the dispersion of the experimental data is further increased. The mechanism of rupture is not different from that of P50 samples, but the values of MOR decrease down to 12 MPa, probably indicating the effect of coalescence of macrocavities, and confirming that for very high porosities the thickness of the cell walls becomes unsuitable to guarantee adequate mechanical properties.

3.3.1. Microhardness and nanoindentation testing

Nanoindentation results for both dense and porous samples are presented in Table 4 and Figs. 3–5, where hardness and modulus vs penetration depth curves are reported.

In case of a dense cylindrical sample with 96% relative density (Fig. 3) both hardness and modulus are constant with penetration depth, and the measured values are close to those found in the literature for bulk zirconia, measured by the same technique.[26]

On the other hand, a decreasing indentation modulus and hardness with penetration depth are observed in case of the prismatic samples (both dense and porous, Figs. 4 and 5, respectively). This apparent indentation size effect (ISE) is likely due to the presence of sub-surface micro-porosity, which significantly affects the mechanical response of the system for a penetration

Fig. 4. Indentation hardness (left axis) and modulus (right axis) vs penetration depth curves for a dense prismatic bar; the intrinsic properties of the ceramic bodies and the influence of micro-porosity on indentation response can be evaluated (statistical processing of 12 indentations).

Fig. 5. Indentation hardness (left axis) and modulus (right axis) vs penetration depth curves for a porous prismatic bar (set P50) (a); hardness vs plastically deformed volume curve for the same sample (statistical processing of 12 indentations) (b).
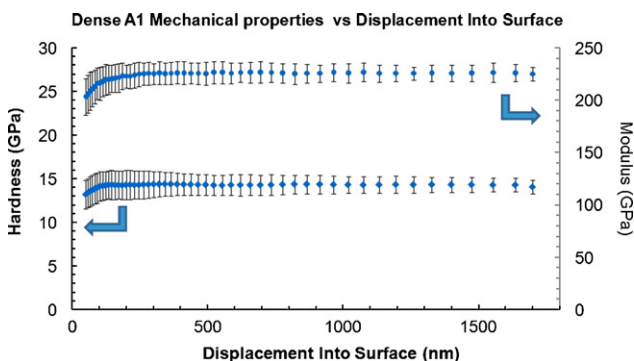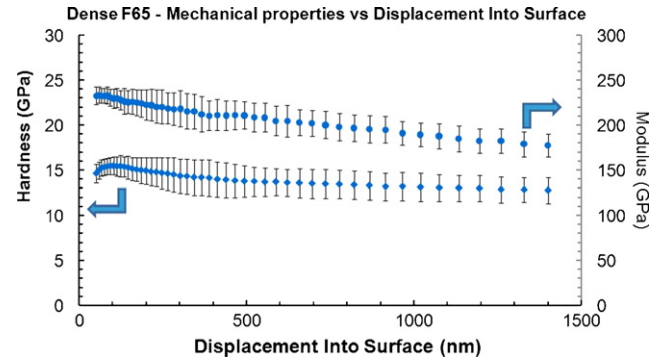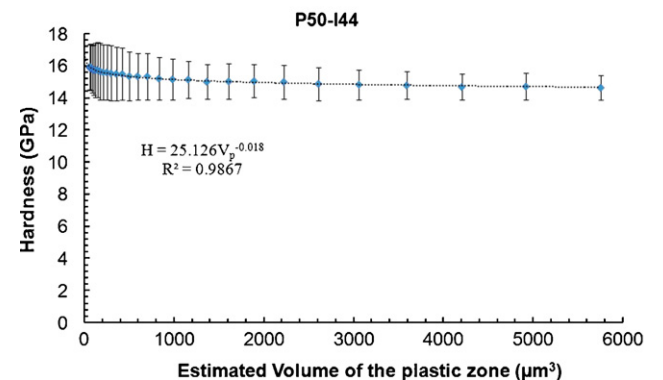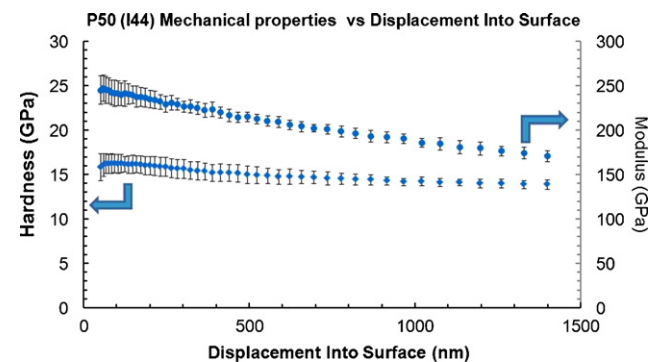

Fig. 3. Indentation hardness (left axis) and modulus (right axis) vs penetration depth curves for a dense cylinder (statistical processing of 12 indentations).
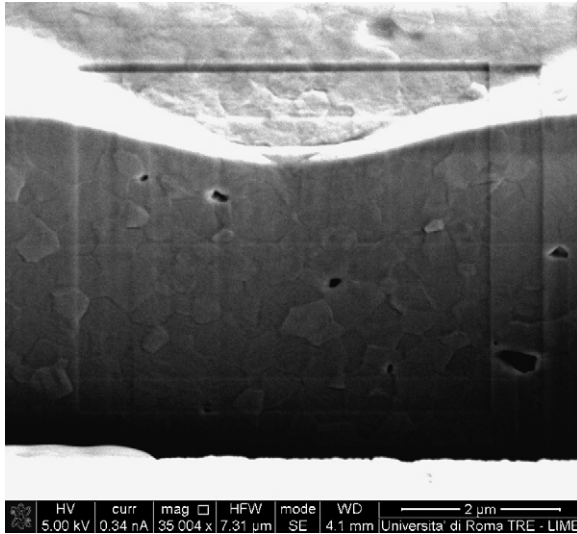
Fig. 6. FIB cross-sectioning of the indented zone of a P50 sample (FEG-SEM micrograph): sub-surface micro-porosity is made evident.

depth higher than 500 nm. As a confirmation, the FIB cross-section of an indentation mark is reported in Fig. 6, where the presence of micro-pores beneath the indentation area is made evident. It is significant that the elastic modulus measured at the maximum load for dense samples (177 GPa) is very close to the one obtained by bending tests (172 GPa), suggesting that the selected scale for nanoindentation (identified by the maximum penetration depth, 1500 nm) is sufficient to take into the due account the effect of micro-porosity on the elastic properties and hardness of samples.

The observed consistency of data coming from nanoindentation and macroscopic bending can be explained only after a careful evaluation of the characteristic interaction volume between sample and adopted mechanical probe in both cases.

To have an idea of the deformed volume in the case of Berkovich nanoindentation, it is useful to consider the plastically deformed volume beneath the indenter, which was found to be approximately hemispherical[27] for a bulk material tested with a pyramidal indenter, with a radius of the plastic zone R_p, given by[27]:

$$R_p = k \cdot \left[\left(\frac{E}{H} \right)^{1/2} \cdot \cot^{1/3} \psi \right] \cdot \delta \tag{4}$$

where k is an indenter specific geometric constant (equal to 3.64 in case of a Berkovich indenter), ψ is the effective indenter angle (70.3° for a Berkovich indenter), and δ is the plastic depth measured during indentation.

In this way, the plastically deformed volume V_p beneath the indentation can be estimated as follows:

$$V_p = \frac{2}{3} \pi R_p^3 \tag{5}$$

It is then possible to estimate directly the mechanical properties as a function of the volume of interaction, which is found to be much greater than the average size of micro-porosity, as reported

in Fig. 5(c), where a power law relationship was also found between measured hardness and deformed plastic volume.

It is important to note that hardness seems to be constant for the highest values of plastic volume (Fig. 5(c)), confirming that the hardness value measured at maximum load is representative of the "microporous" ceramic body, while the mechanical properties measured at the lowest penetration depths are representative of the intrinsic properties of zirconia.

This observation explains why data coming from nanoindentation at high penetration depth are very close to the one obtained by macroscopic bending, being the typical interaction volume in both cases significantly higher than the mean size of microporosity. As a consequence, by the knowledge of the hardness gradient a rough estimation of the sub-surface micro-porosity amount is also possible, using a simple rule of mixture:

$$H_{\min} = \frac{V_{ZrO_2}}{V} \cdot H_{\max} \tag{6}$$

where $H_{\max}$ is the intrinsic hardness of the bulk zirconia, calculated at a penetration depth of 100 nm, and $H_{\min}$ is the minimum hardness value, calculated at maximum penetration depth.

A surface micro-porosity value of about 12% is estimated for both dense and porous samples, which is slightly higher than the one estimated (7%) by weight/volume measurement on the dense sample, meaning that micro-porosity is mostly concentrated near the surface during the densification and de-airing processes. As a confirmation, the FIB section reported in Fig. 6 clearly shows a wide presence of micropores beneath the surface, which has been roughly estimated of the order of 10% by Image Analysis.

3.4. Implementation of DIB-FEA

The binarized images of macro-porous samples, converted into a representation of a bi-phasic structure (consisting of "solid PSZ" and "pores"), were shown in Fig. 1. A computational mesh (initially entirely made of triangular elements) was generated from these binary maps and iteratively refined (introducing smaller and tetrahedral elements) to adapt it to the calculation requirements.

The final value of homogeneity, defined as the ratio between the areas occupied in each one of the elements by the two phases, gives an indication of the suitability of the generated structure to represent accurately the actual microstructure. A computational mesh derived from the binarization of the digital image shown in Fig. 1(d) (P50 set 2), made of 17,256 elements and characterized by a total homogeneity of 99%, is shown in Fig. 7.

Experimental values of the mechanical properties must be assigned to the individual phases to proceed to the calculation. For the PSZ phase, the assigned value of elastic modulus for the simulation of the application of a compressive load can either be derived from the results of nanoindentation (provided that the presence of the micropores is properly taken into account) or from the results of macro-mechanical tests: considering the very good accordance between high load nanoindentation and macroscopic bending tests, a value of 180 GPa was assigned to the "microporous" PZS phase, even if neither of the two testing
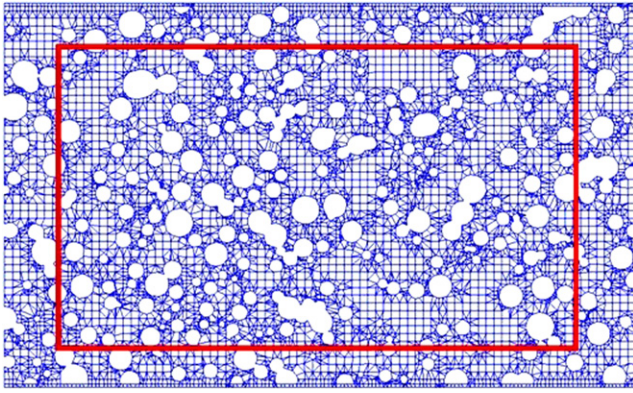
Fig. 7. Computational mesh (17,256 elements, 99% homogeneity) representing the binary image in Fig. 1(d) (P50-2): the solid line confines the area that was actually selected for the simulation of the mechanical behavior; realistic boundary conditions were simulated by the presence of the area lying outside the solid line.

methods reproduces exactly the loading conditions that have to be simulated (uniaxial compression).

The boundary conditions were selected to minimize the influence of the border: only the central part of the micrograph was considered for the simulation, so that the loading conditions applied to the border are physically realistic (see rectangular area in Fig. 7).

To simulate the application of the load, a fixed joint constraint was assigned to the lower surface, while a length variation of −10% was imposed to the mesh. The model allows to calculate in plane strain values (ε_x and ε_y) experienced in each node of the mesh. By substitution of calculated strain components in the Hooke's law for plane strain:

$$E_{\text{cellular}} = \frac{(\sigma_{yy}[(1+\nu)(1-2\nu)])}{(\nu\varepsilon_x + (1-\nu)\varepsilon_y)} \tag{7}$$

where ν is the Poisson ratio, the elastic modulus E_{cellular} of the cellular material can be obtained. For the examined case, a value of $E_{\text{cellular}} = 50.7$ GPa was calculated.

Moreover, the distribution of the intensity of the stress, σ_{yy}, within the structure can be evidenced (see Fig. 8), confirming that the areas that develop the highest stresses as a consequence of the uniform application of an uniaxial load are those characterized by the thinnest walls among cavities.
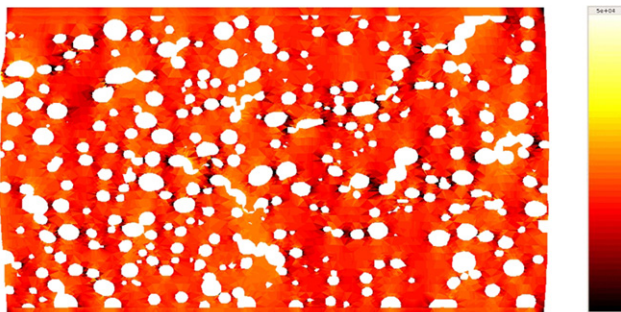

Fig. 8. Results of the simulation of the application of an uniaxial compressive load to a P50-2 sample: colorimetric map of the σ_{yy} stress intensity distribution.

Table 5
Elastic modulus of P50 and P65 cellular ceramics: comparison between experimental results (from uniaxial compression tests) and calculated values (from DIB-FE analysis).

Samples	Density %	Elastic modulus experimental (±st. dev.) GPa	Elastic modulus calculated (±st. dev.) GPa
P50 set 1	59.7	45.6 ± 5.8	50.7 ± 3.7
P50 set 2	63.3	43.3 ± 15.4	44.2 ± 3.6
P65	49.2	10.7 ± 3.5	12.6 ± 1.1

However, FIB-SEM microstructural analyses showed that also micro-porosity could play a fundamental role in determining the actual stress distribution within the porous structure. Therefore, the modeled stress distribution must be considered as a qualitative estimation of the stress rearrangement due to macroporosity.

Table 5 reports a direct comparison between the experimental results obtained from the mechanical characterization (uniaxial compression tests) and the results of the DIB-FEA implementation carried out on 5 different representative sections for each experimental set.

The following observations apply: (i) the dispersion of the calculated E values is much lower than that of the corresponding experimental data gathered from mechanical tests; (ii) a good agreement can be found between experimental results and predicted values of elastic modulus: the highest difference (about 12% of the value) is relative to P65 samples, that are characterized by the highest dispersion of the results of mechanical tests; (iii) the simulations confirmed that samples P50 from set 1, characterized by an uneven microstructure (with evident coalescence of the large pores), that would hardly make them acceptable for final applications, exhibit, however, mechanical properties very similar to those of samples P50 from set 2, whose microstructural features, in terms of overall homogeneity, are certainly superior.

4. Conclusions

The following conclusions can be drawn from gathered experimental evidence and further elaborations:

- ceramic materials obtained by gel casting of yttria partially stabilized zirconia powders are characterized by about 7 vol.% residual micro-porosity from thermal degradation of the gelling agent and subsequent sintering of ceramic powders; an elastic modulus of about 170 GPa and a modulus of rupture of about 400 MPa were measured for samples obtained without the addition of pore forming agents.
- The amount, size and distribution of macroporosity of cellular ceramics can be strictly controlled by correctly selecting the size of pore forming agents (polyethylene spheres for the presented materials) and by optimizing their dispersion in the gelling agent; about 50% and 65% porous cellular materials were obtained, with very even distribution of mainly spherical cavities with diameters ranging from about 120 to 350 μm.

- Nanoindentation testing was successfully applied for the evaluation of intrinsic properties of the PZS dense phase. A deeper analysis of the modulus/depth curves, supported by FIB-SEM microstructural characterization, also allowed to give a semi-quantitative estimation of the influence of micro-porosity on mechanical properties, and a very good accordance with elastic modulus results from bending tests was evidenced.
- The mechanical properties of cellular ceramics produced by gel casting are mostly influenced by the total amount of pores, rather than by the distribution of the cavities inside the solid matrix.
- DIB-FEA simulation of the mechanical behavior implemented starting from SEM micrographs of representative cross-sections gave rise to very reliable predictions of elastic properties, provided that the influence of micro-porosity were properly taken into account by assuming an average modulus for the PSZ phase: elastic moduli only 5–10% different from the corresponding measured values were calculated for cellular ceramics produced with different amounts of pores and in different conditions.
- Microstructural FIB-SEM analyses showed that the actual geometry of pores at microscale and nanoscale was significantly different from the spherical one, and a strong influence of micro-porosity on damage mechanisms and failure modes is expected. For these reasons, the implemented models could not be used to produce reliable strength and/or toughness predictions.

A present limitation of the simulation procedure can therefore be found in the practical impossibility (due to excessively onerous computing effort and to the limits in the resolution of digital images) of taking into account simultaneously, in one single calculation, microstructural features of different orders of magnitude, such as micropores deriving from incomplete sintering and macropores or other macro-defects generated by the presence of pore forming agents.

Positive advantages can be derived from the application of DIB-FEA methods to cellular materials by the possibility of creating direct real correlations between specific microstructural features and overall mechanical elastic properties, thus allowing to reduce the number of material developing cycles and to improve the fabrication process minimizing safety coefficients during components design.

Acknowledgements

References

1. Scheffler, M. and Colombo, P., ed., *Cellular ceramics, structure, manufacturing, properties and applications*. Wiley-VCH Verlag GmbH & Co, Weinheim, Germany, 2005.
2. Studart, A. R., Gonzenbach, U. T., Tervoort, E. and Gauckler, L. J., Processing. Routes to macroporous ceramics—a review. *Journal of the American Ceramic Society*, 2006, **89**(6), 1771–1789.
3. Colombo, P., Conventional and novel processing methods for cellular ceramics. *Philosophical Transactions of the Royal Society A*, 2006, **364**, 109–124.
4. Lopes, R. A. and Segadaes, A. M., Microstructure, permeability and mechanical behavior of ceramic foams. *Materials Science and Engineering A*, 1996, **209**, 149–155.
5. Han, Y., Li, J., Wei, Q. and Tang, K., The effects of sintering temperatures on alumina foam strength. *Ceramics International*, 2002, **28**, 755–759.
6. Gibson, L. J. and Ashby, M. F., *Cellular solids: structure and properties*. Cambridge University Press, Cambridge, UK, 1999.
7. Kumar, R. S. and McDowell, D. L., Generalized continuum modeling of 2-D periodic cellular solids. *International Journal of Solids and Structures*, 2004, **41**, 7399–7422.
8. Wang, A. J. and McDowell, D. L., In-plane stiffness and yield strength of periodic metal honeycombs at intermediate relative density. *ASME Journal of Engineering Materials and Technology*, 2004, **126**, 137–156.
9. Hollister, S. J. and Kikuchi, N., Homogenization theory and digital imaging: a basis for studying the mechanics and design principles of bone tissue. *Biotechnology and Bioengineering*, 1994, **43**(7), 586–596.
10. Terada, K., Miura, T. and Kikuchi, N., Digital image-based modeling applied to the homogenization analysis of composite materials. *Computational Mechanics*, 1997, **20**(4), 331–346.
11. Terada, K., Hori, M., Kyoya, T. and Kikuchi, N., Simulation of the multi-scale convergence in computational homogenization approach. *International Journal of Solids and Structures*, 2000, **37**(16), 2285–2311.
12. Reid, A. C. E., Langer, S. A., Lua, R. C., Coffman, V. R., Haan, S. I. and Garcia, E., Image-based finite element mesh construction for material microstructures. *Computational Materials Science*, 2008, **43**(4), 989–999.
13. Carter, W. C., Langer, S. A. and Fuller, E. R., The OOF Manual: version 1.0, National Institute of Standards and Technology, NISTIR No. 6256, 1998.
14. Klett, J. W., McMillan, A. D., Gallego, N. C. and Walls, C. A., The role of structure on thermal properties of graphitic foams. *Journal of Materials Science*, 2004, **39**, 3659–3676.
15. Cannillo, V., Manfredini, T., Montorsi, M. and Boccaccini, A. R., Investigation of the mechanical properties of Mo-reinforced glass–matrix composites. *Journal of non-Crystalline Solids*, 2004, **334**, 88–93.
16. http://www.ctcms.nist.gov/oof/.
17. Omatete, O. O., Janney, M. A. and Strehlow, R. A., Gelcasting—a new ceramic forming process. *American Ceramic Society Bulletin*, 1991, **70**(10), 1641–1649.
18. Vandeperre, L. J., De Wilde, A. M. and Luyten, J., Gelatin gelcasting of ceramic components. *Journal of Materials Processing Technology*, 2003, **135**, 312–316.
19. Millan, A. J., Nieto, M. I., Moreno, R. and Baudin, C., Thermogelling polysaccharides for aqueous gelcasting-part III: mechanical and microstructural characterization of green alumina bodies. *Journal of European Ceramic Society*, 2002, **22**, 2223–2230.
20. Lombardi, M., Montanaro, L., Grémillard, L. and Chevalier, J., New gelcasting procedure to prepare alumina porous components: process optimization and preliminary mechanical tests, In *Proceedings of the 32nd international conference & exposition on advanced ceramics and composites*, ed. R. Narayan and P. Colombo. Daytona Beach (FL), 2008.
21. Tulliani, J. M., Bartuli, C., Bemporad, E., Naglieri, V. and Sebastiani, M., Preparation and mechanical characterization of dense and porous zirconia produced by gel casting with gelatine as a gelling agent, *Ceramics International*, 2009, http://dx.doi.org/10.1016/j.ceramint.2009.02.017, in press.
22. Xie, Z. P., Yang, J. L., Huang, D., Cheng, Y. L. and Huang, Y., Gelation forming of ceramic compacts using agarose. *British Ceramic Transactions*, 1999, **98**(2), 58–61.
23. Oliver, W. C. and Pharr, G. M., Measurement of hardness and reduced modulus by instrumented indentation: Advances in understanding and

refinements to methodology. *Journal of Materials Research*, 2004, **19**(1), 3–20.

24. Kardestuncer, H., *Finite elements handbook*. McGraw-Hill, New York, USA, 1987.

25. Zimmermann, A., Hoffman, M., Flinn, B. D., Bordia, R. K., Chuang, T.-J., Fuller Jr., E. R. *et al.*, Fracture of alumina with controlled pores. *Journal of American Ceramic Society*, 1998, **81**(9), 2449–2457.

26. Luo, J. and Stevens, R., Porosity-dependence of elastic moduli and hardness of 3Y-TZP ceramics. *Ceramics International*, 1999, **25**, 281–286.

27. Chen, J. and Bull, S. J., On the relationship between plastic zone radius and maximum depth during nanoindentation. *Surface & Coatings Technology*, 2006, **201**, 4289–4293.